Online Supplemental Material for

J. Gen. Physiol. Vol. 117 No. 6 p. 583, Lingle et al.

Additional Evaluation of Predictions from Scheme 1 and Scheme 2

Christopher J. Lingle, Xu-Hui Zeng, Jui-Ping Ding, and Xiao-Ming Xia

Predictions for Steady-state and Tail Current G-V Curves Arising from Scheme 1 and Scheme 2

Predicted steady-state and tail current G-V curves were determined based on Eqs. 5 and 6 of the main article, for a range of Ca^{2+} concentrations for both Scheme 2 A (Fig. S1 A) and Scheme 1 (Fig. S1 B). Values for relevant parameters in Eqs. 5 and 6 are provided in the figure legend. The predicted tail current G-V curves arising from channels in the absence of inactivation are also compared with the predicted tail current G-V curves for Scheme 2 (Fig. S1 C) and Scheme 1 (Fig. S1 D). In both blocking models, because channels in inactivated states, I_n, unblock rapidly enough to contribute to the tail currents, the predicted tail current G-V curves are shifted relative to that expected for activation of the channels in the absence of inactivation. A second unusual property of the predicted tail current G-V curves is that their steepness is increased relative to that expected based on the activation equilibrium alone. This results from the contribution of the voltage dependence of occupancy of the blocked states that are unblocked during repolarization. Thus, when rapid unblocking contributes to peak tail current, estimates from tail currents of the voltage of half activation and voltage dependence do not solely reflect activation properties of the underlying channels.

Fig. S1 E compares the $V_{0.5}$ for activation based on Scheme 1, Scheme 2, and the activation equilibrium alone in the absence of inactivation. For both blocking schemes, the apparent half activation voltage is shifted to more negative potentials particularly at lower Ca^{2+}. The magnitude of the shift produced by each blocking mechanism is plotted as a function of Ca^{2+} in Fig. S1 E, emphasizing the larger effect at lower Ca^{2+}. At elevated Ca^{2+}, there remains a relatively Ca^{2+}-independent shift in the $V_{0.5}$ relative to that with no inactivation. The exact magnitude of the shift is dependent on the particular parameters of the blocking equilibrium and its voltage dependence. Thus, irrespective of the blocking model used, the rapid recovery from blocked states can produce an apparent shift in the $V_{0.5}$ for activation, when measured using tail currents. This effect is qualitatively similar to the apparent shift in $V_{0.5}$ resulting from coexpression of $\alpha + \beta 3b$ subunits that is observed over all Ca^{2+} concentrations (Xia et al., 2000).

To evaluate the usefulness of macroscopic conductance measurements in discriminating between different blocking models, idealized G-V curves predicted from Scheme 2 were fit with either a Scheme 1 or Scheme 2 formulation (not shown), and the idealized curves determined from Scheme 1 were similarly fit (not shown). In the case of simulated G-V curves generated by Scheme 2, fitting with Scheme 1 resulted in a fit that, with a real data set, would be considered perfectly adequate. When the conductance values generated by Scheme 1 were fit with a Scheme 2 model, not unexpectedly the extra free parameters allowed a perfect fit, although some of the parameters were not well-defined. This exercise indicates that, even when simultaneously fitting both steady-state and tail current G-V curves, measured over a range of Ca^{2+} concentrations, such measurements are of limited use in discriminating between Scheme 1 and Scheme 2.

Simulation of Current Activation

Examples of current families activated in accordance with Scheme 2 for 0, 1, 10, and 300 μM Ca^{2+} are shown in Fig. S2. The currents provide a reasonable approximation of those observed experimentally (Fig. 1 of main article), although some discrepancies exist. As already noted, the simulated currents exhibit a similar amount of steady-state current at the most positive activation voltages for all Ca^{2+}, in contrast to the actual currents which exhibit reduced current at low Ca^{2+}. Furthermore, with the sets of rates we have used, the apparent activation rate of currents at low Ca^{2+} is slower than observed experimentally. With faster inactivation rates, it was possible to increase the apparent activation rates at lower Ca^{2+}, but at the expense of producing too much macroscopic inactivation at higher Ca^{2+}. Since the 10-state MWC model fails to account for many aspects of *Slo* behavior at 0 Ca^{2+} (Nimigean and Magleby, 2000; Rothberg and Magleby, 2000; Talukder and Aldrich, 2000), some of the difficulties of the two-step blocking model in accounting for behavior at lower Ca^{2+} may arise from the limitations of the activation model. Despite this limitation, the G-V curves resulting from the simulated currents mirror the general properties of the tail, steady-state, and peak G-V curves (Fig. S2 B) observed for the native currents (Fig. 1, main article). In addition, the tail

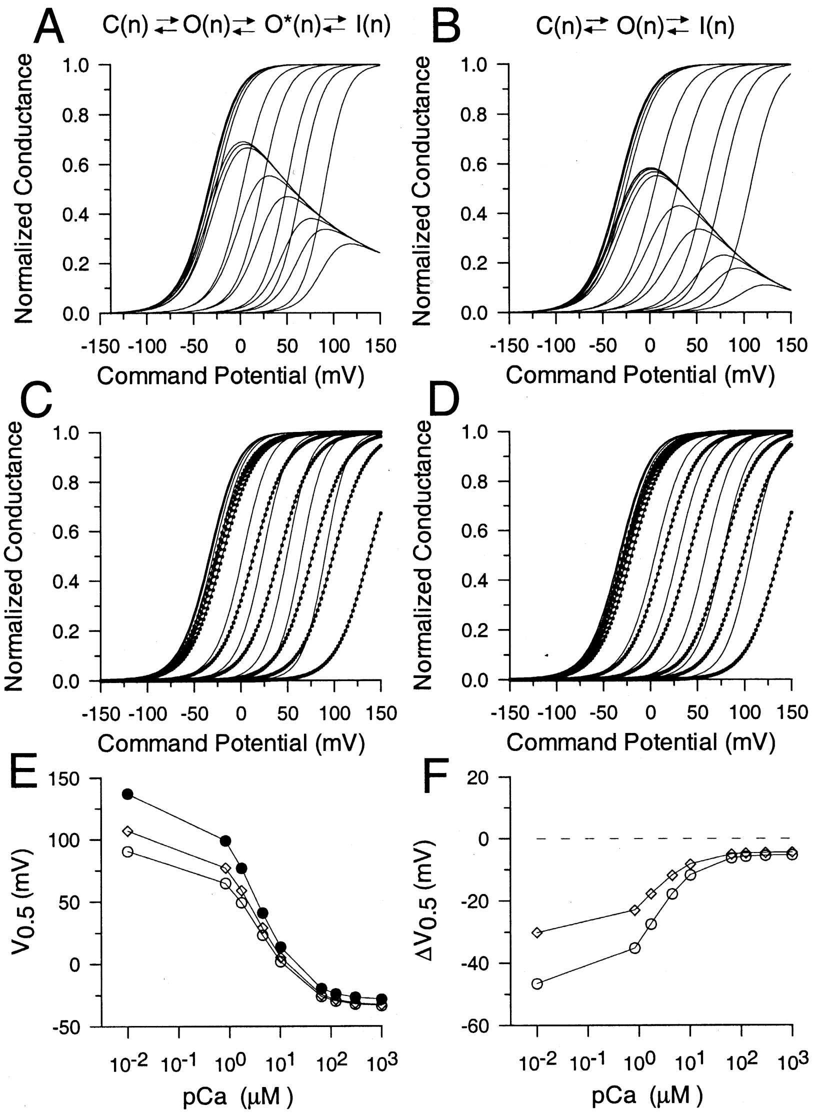

FIGURE S1. Comparison of expected G-V behavior for Scheme 2 and Scheme 1. In A, predicted G-V curves for Scheme 2 were generated as described in MATERIALS AND METHODS and RESULTS based on Eq. 5 (steady-state currents) and Eq. 8 b (tail currents) of the main article. For tail current G-V curves, channels in states O, O*, and I at the time of the tail current were assumed to contribute to the peak tail current. For steady-state current, channels in states O and O* were assumed to contribute to the steady-state current. Parameters used for Eqs. 5 and 6 were KC = 10, $K_O = 1$, $L(0) = 2{,}000$, and $Q = 1.4e$. For the $O \rightleftharpoons O^*$ equilibrium, $K_1 = 0.4152$ with $Q_1 = 0.6315e$. For the $O^* \rightleftharpoons I$ equilibrium, $K_2 = 1$, $Q_2 = 0.20208e$. For all panels, Ca^{2+} concentrations were 0, 0.84, 1.7, 4.5, 10.2, 65, 124, and 300 μM and 1 and 3 mM. In B, G-V curves were similarly calculated from Scheme 1 for the case where recovery from I to O was assumed to be extremely rapid at the potential of the tail currents. Thus, tail current was assumed to arise from occupancy of I and O at the time of the tail current, whereas steady-state current arose from occupancy of state O alone. Activation values were as in A, while $K_1 = 0.509$ and $Q_1 = 0.505e$. In C, tail current G-V curves from Scheme 2 are compared with tail currents expected for channels opening with the same activation behavior but lacking the blocking mechanism (lines with dots). The presence of an intact blocking mechanism results in steeper G-V curves and also substantially shifts the apparent $V_{0.5}$ to more negative activation potentials at a given Ca^{2+}. In D, G-V curves from Scheme 1 and from the closed-open equilibrium in the absence of inactivation are compared. As in B, the presence of the blocking mechanism results in a leftward shift in the apparent $V_{0.5}$ for activation with an increase in the apparent voltage dependence of activation. In E, the $V_{0.5}$ calculated from the tail G-V curves in panels C and D are plotted for Scheme 1 (◇), Scheme 2 (○), and in the absence of inactivation (●). The magnitude of the shift resulting from the blocking mechanism diminishes with elevations in Ca^{2+}. In F, the change in $V_{0.5}$ relative to the $V_{0.5}$ in the absence of inactivation is plotted for both Scheme 2 (○) and Scheme 1 (◇). The magnitude of the shifts in $V_{0.5}$ is dependent on the values of the blocking constants in the simulations.

current G-V curves exhibit the shift in apparent voltage dependence (Fig. S2 C) and shift in $V_{0.5}$ at low Ca^{2+} (Fig. S2 D) expected for this model.

Can Scheme 1 predict the families of currents activated at different Ca^{2+}? Fitting of the families of G-V curves with Scheme 1 resulted in an estimate for the blocking equilibrium of $K(V) = 0.71e^{0.34FV/RT}$. If one assigns a zero voltage forward rate of 500/s and a zero voltage unblocking rate of 700/s, this will result in macroscopic currents with inactivation time constants of ~0.8–0.5 ms over the range of 0 to +180 mV. This results in a fractional block of peak current and time constants of inactivation that are similar to those observed experimentally. However, with these rates and voltage dependencies, the tail currents upon repolarization will not exhibit any "instantaneous" component of unblock, instead showing only a large unblocking tail occurring with a time constant of ~180 μs at −100 mV. If the unblocking rate or its voltage dependence is altered to allow the occurrence of "instantaneous" unblocking, then the amount of steady-state current at positive activation potentials is not correctly described. Thus, unlike Scheme 2 (Fig. S2), there is no set of parameters for the blocking reaction in Scheme 1 that can result in both the properties of the outward currents and the tail currents seen, for example, in Figs. 1 and 2 of the main text.

Simulation of Deactivation

We have noted that both Scheme 1 and Scheme 2 predict some prolongation of the deactivation time constant (τ_d) relative to currents lacking an inactivation mechanism. Yet, this prolongation is not observed. To examine this more directly, currents were simulated using a standard deactivation protocol with different Ca^{2+} concentrations (Fig. S3 A). Over all Ca^{2+}, the tail currents exhibit the characteristic nonohmic rapid unblock, whereas at higher Ca^{2+} there is the characteristic unblocking relaxation. However, measurement of the empirical τ_d for such simulated currents reveals discrepancies from the properties of the actual currents. Specifically, for the 10-state MWC activation model, the dependence of τ_d on membrane potential (Fig. S3 B) shows that, as Ca^{2+} is elevated, there is a characteristic slowing of deactivation. In contrast, with the rates given in Table I, Scheme 2 yields currents in which τ_d exhibits only a minimal prolongation with elevations in Ca^{2+} (Fig. S3 C). This stems from the fact that deactivation is being rate limited by the unblocking transitions. By increasing the value of k_r such that channels in O^*_n more rapidly return to O_n, τ_d for currents stimulated with Scheme 2 can begin to more closely approximate τ_d for

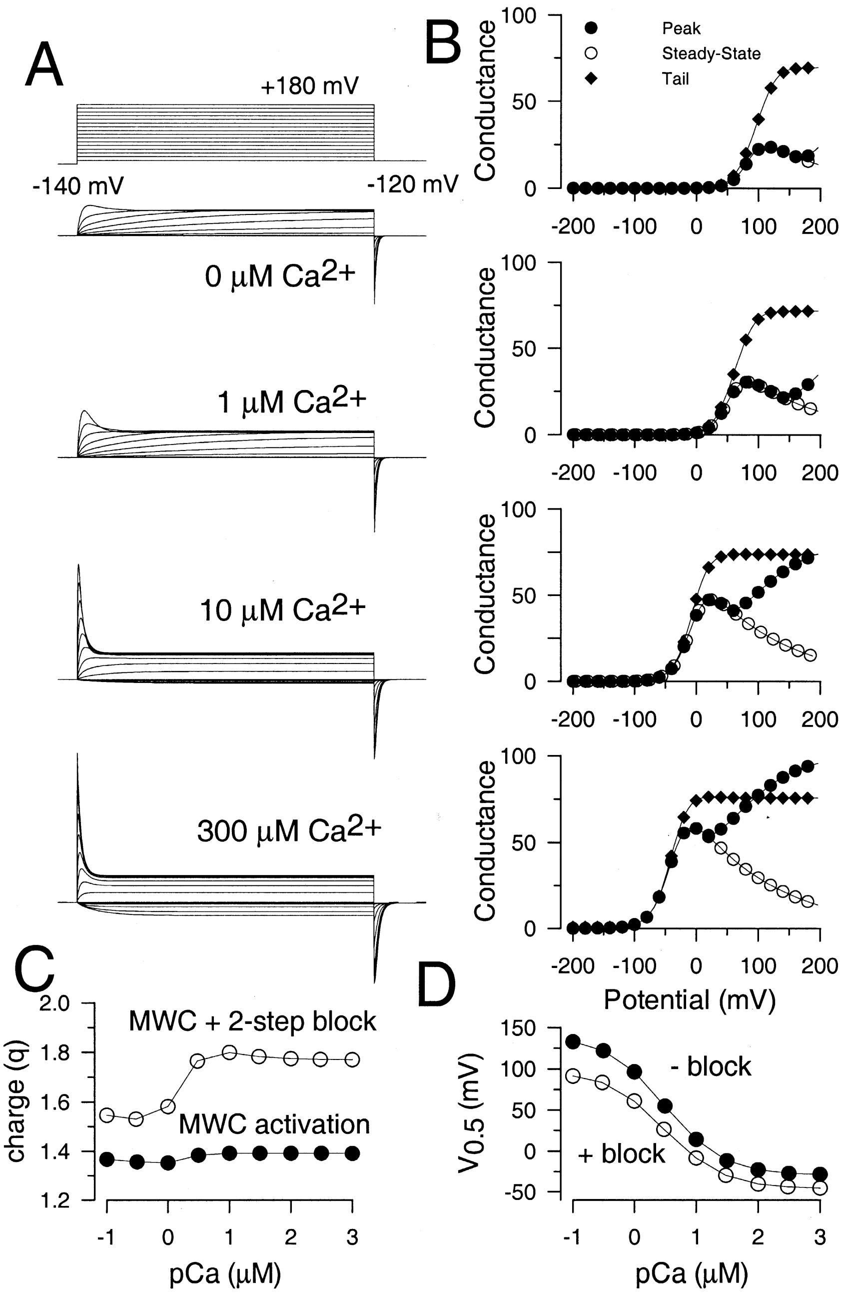

FIGURE S2. Current activation predicted by Scheme 2 using rates in Table I. In A, traces show predicted currents at 0, 1, 10, and 300 μM Ca^{2+} activated at voltages from −180 to +180 mV after 40 ms at −120 mV. Currents were simulated using Scheme 2 in conjunction with a 10-state MWC activation model (Cox et al., 1997). Rates for activation and block are given in Table I. In B, conductance-voltage curves were generated from the peak, steady-state, and tail currents from traces shown in A at each Ca^{2+} concentration. In C and D, to obtain estimates of net charge and $V_{0.5}$, single Boltzmann function (Eq. 1) was fit to the tail current G-V curve over a range of Ca^{2+} concentrations channels activated in accordance with the values in Table I either with or without the blocking steps. In C, the net charge is plotted as a function of Ca^{2+}. In D, the $V_{0.5}$ obtained from the tail currents is plotted for both the currents activated by the 10-state MWC model and those activated and inactivated in accordance with Scheme 2.

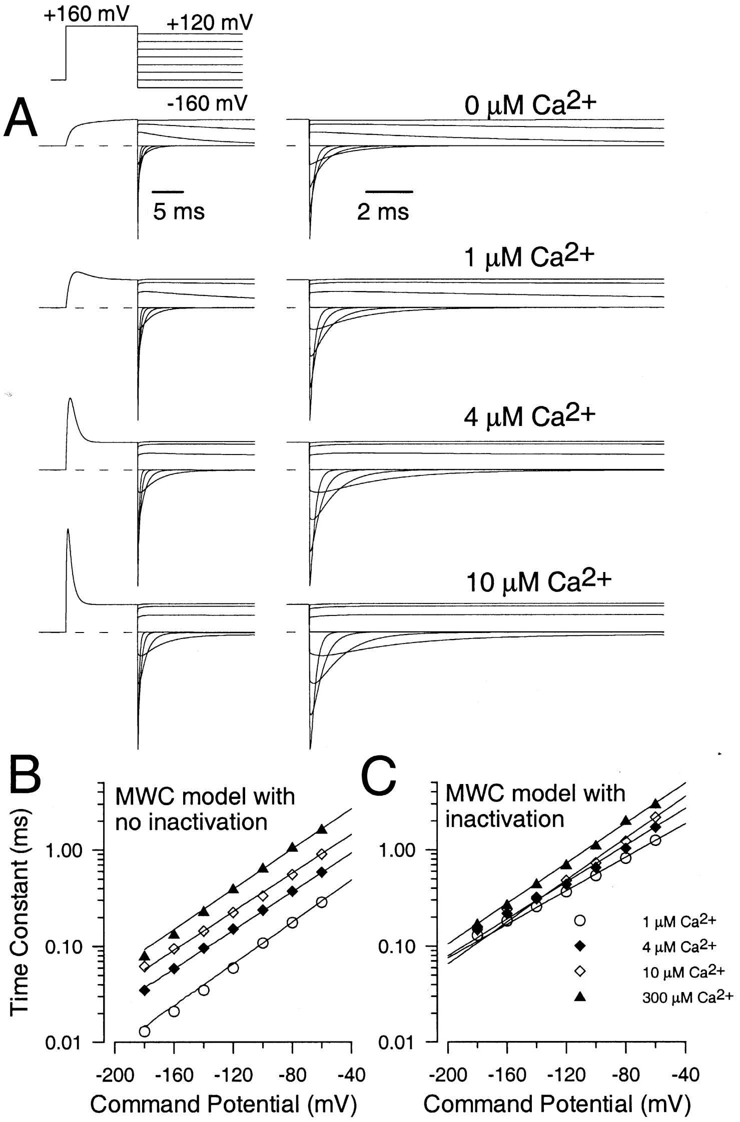

FIGURE S3. Scheme 2 results in a deactivation time course containing both instantaneous and slower components of unblocking. In A, currents were simulated using the parameters in Table I (main article) with the voltage protocol shown on the top for the indicated Ca^{2+} concentrations. Expanded time base traces on the right show that, upon repolarization, there is an initial rapid nonohmic step in current followed by a shoulder or, in some cases (e.g., −80 mV at 10 µM Ca^{2+}), an increase in current before the onset of an exponentially decaying tail current. The shoulder in the tail current is more pronounced at higher $[Ca^{2+}]$. In B, time constants for deactivation over a range of potentials are plotted for currents generated as in A, but with only the 10-state MWC model (no inactivation). In C, deactivation time constants from tail currents from traces as in A are plotted as a function of tail current potential over a range of $[Ca^{2+}]$. With the rates given in Table I, τ_d is strongly influenced by the transition from O* to O.

the 10-state MWC model. However, in such a case, other properties of the resulting current, e.g., unblocking in the tail current and the properties of τ_i, begin to deviate from what is observed.

The Two-step Blocking Model May Explain the Inability of a Cytosolic Blocker to Hinder the Inactivation Process

The application of cytosolic TEA at a concentration that results in over a 50% reduction of α + β3b current fails to alter the time course of the inactivation process (Xia et al., 2000). A similar result has been observed with the β2 subunit (Xia et al., 1999) and native inactivating BK channels in chromaffin cells (Solaro et al., 1997). These results suggest that the inactivation domains of the β2 and β3 subunits may not bind directly to a site in the channel that can be occupied by cytoplasmic channel blockers.

Here we examine expectations of how a cytosolic blocker might affect channels inactivating with the proposed two-step inactivation model. We have considered three cases: (1) binding of TEA to either O or O*, with no effect on the ability of O to passage to O* (Fig. S4 A); (2) binding only to O* (Fig. S4 B); and (3) binding only to O (Fig. S4 C). The rates of block by TEA were set to be very rapid compared with the transitions between O and O*, but comparable to those between O* and I. Only in the cases where TEA effectively buffers entry from O into O* (Fig. S4 C) is there a competitive slowing of the inactivation process. In contrast, when TEA binds to either open state, but does not impede movement to O* (Fig. S4 A), TEA has essentially no effect on the time course of the inactivation process. This results from the fact that the rate-limiting step in the inactivation process is defined by O → O* which is not impaired by the binding of TEA. The inability of one category of model to slow the inactivation pro-

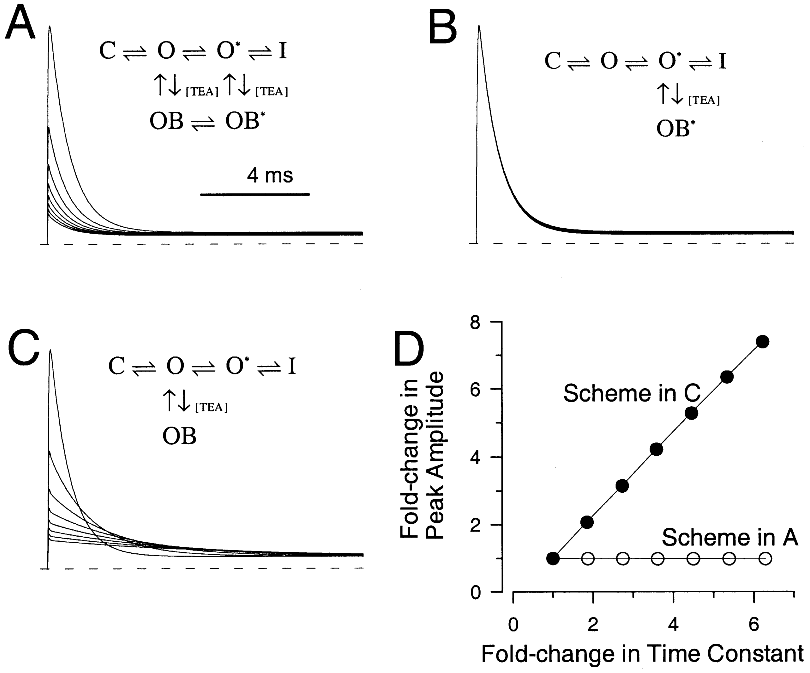

FIGURE S4. The two-step blocking model may account for the failure of cytosolic blockers to impede inactivation. Currents were simulated with a simplified activation model ($\mathrm{C} \leftrightarrows \mathrm{C} \leftrightarrows \mathrm{C} \leftrightarrows \mathrm{O}$) with the addition of the indicated blocking steps. TEA concentrations were 0, 0.5, 1, 1.5, 2.0, 2.5 and 3.0 mM. The forward rate of TEA block was set to $10^7\ \mathrm{M}^{-1}\mathrm{s}^{-1}$ ($z = 0.46$) and the unblocking rate was 100,000/s ($z = -0.316$). The command step was to +100 mV. Thus, the rates were very rapid compared with the transitions between O and O*, but comparable to those between O* and I. In A, TEA can bind to either open state, but binding of TEA does not impede movement from O to O* and no slowing of inactivation is observed. In B, TEA binds only to O*. The essential absence of a TEA effect except for the steady-state currents reflects the fact that once the channels reach O* they become nonconducting either by transitions to I or O. The channels therefore are spending minimal time in O*. In C, binding of TEA only to O results in the typical slowing of inactivation characteristic of simple block schemes. In D, the changes in amplitude as a function of changes in time constant are plotted for the blocking schemes in A and C.

cess and one to impede it is summarized in Fig. S4 D, in which the fold change in the current amplitude observed with two different schemes is plotted as a function of the change in time constant.

This analysis provides a possible explanation of why competition between cytosolic blockers and the inactivation process is not observed with the β3b subunit (and possibly the β2 subunit). Thus, although TEA might conceivably bind to a site that inhibits the movement of the inactivation domain into its inactivating position, this could in essence be a kinetically silent effect. This result leaves open the possibility that the final blocking position of the inactivation domain is, in fact, at the mouth of the BK ion permeation pathway. However, it does not prove that possibility, and it remains possible that TEA simply does not interact with either the binding or blocking steps of the β2 or β3b subunits.

REFERENCES

Cox, D.H., J. Cui, and R.W. Aldrich. 1997. Allosteric gating of a large conductance Ca-activated K^+ channel. *J. Gen. Physiol.* 110:257–281.

Nimigean, C.M., and K.L. Magleby. 2000. Functional coupling of the β(1) Subunit to the large conductance Ca^{2+}-activated K^+ channel in the absence of Ca^{2+}. Increased Ca^{2+} sensitivity from a Ca^{2+}-independent mechanism. *J. Gen. Physiol.* 115:719–736.

Rothberg, B.S., and K.L. Magleby. 2000. Voltage and Ca^{2+} activation of single large-conductance Ca^{2+}-activated K^+ channels described by a two-tiered allosteric gating mechanism. *J. Gen. Physiol.* 116:75–99.

Solaro, C.R., J.P. Ding, Z.W. Li, and C.J. Lingle. 1997. The cytosolic inactivation domains of BK_i channels in rat chromaffin cells do not behave like simple, open-channel blockers. *Biophys. J.* 73:819–830.

Talukder, G., and R.W. Aldrich. 2000. Complex voltage-dependent behavior of single unliganded calcium-sensitive potassium channels. *Biophys. J.* 78:761–772.

Xia, X.M., J.P. Ding, and C.J. Lingle. 1999. Molecular basis for the inactivation of Ca^{2+}- and voltage-dependent BK channels in adrenal chromaffin cells and rat insulinoma tumor cells. *J. Neurosci.* 19:5255–5264.

Xia, X.-M., J. Ding, X.-H. Zeng, K.-L. Duan, and C. Lingle. 2000. Rectification and rapid activation at low Ca^{2+} of Ca^{2+}-activated, voltage-dependent BK currents: consequences of rapid inactivation by a novel β subunit. *J. Neurosci.* 201:4890–4903.